Supplementary Information

Biomineralization-mimicking cooperative assembly for tailoring anisotropic hierarchically porous metal–organic frameworks

Ruigang Sun,[a] Ji Han,[a] Bin Zhao,[a] Bohan Liu,[a] Guangrui Chen,[ab] Haidong Xu,[a] Baiqi Wang,[a] Yanjing Gao,[a] Song Lin Zhang,[c] Yusuke Yamauchi,[def] and Buyuan Guan*[ab]

a. State Key Laboratory of Inorganic Synthesis and Preparative Chemistry, College of Chemistry, Jilin University, Qianjin Street 2699, Changchun 130012, P. R. China

b. International Center of Future Science, Jilin University, Qianjin Street 2699, Changchun 130012, P. R. China

c. Institute of Materials Research and Engineering (IMRE), Agency for Science, Technology and Research (A*STAR), 2 Fusionopolis Way, Singapore 138634, Singapore

d. School of Chemical Engineering and Australian Institute for Bioengineering and Nanotechnology (AIBN), The University of Queensland, Brisbane QLD 4072, Australia

e. Department of Materials Process Engineering, Graduate School of Engineering, Nagoya University, Furo-cho, Chikusa-ku, Nagoya, Aichi, 464-8603, Japan

f. Department of Chemical and Biomolecular Engineering, Yonsei University, 50 Yonseiro,

Seodaemun-gu, Seoul 03722, Republic of Korea

[*] E-mail: guanbuyuan@jlu.edu.cn

Table of Contents

Section 1. Supplementary Methods

Chemicals

Commercial reagents were purchased and used as received unless otherwise noted. Zirconyl chloride octahydrate ($ZrOCl_2 \cdot 8H_2O$, 99.9% metals basis, Aladdin), zirconium chloride ($ZrCl_4$, 99.9% metals basis, Aladdin), sodium bromide (NaBr, 99%, Aladdin), 2-aminoterephthalic acid (BDC-NH_2, 98%, Aladdin), Pluronic® F-127 (F127, M_w = 12600, Sigma-Aldrich), sodium dodecyl sulfate (SDS, 99%, Sigma-Aldrich), octadecyl dimethyl betaine (ODMB, 30% active matter, Chengdu Ruisi Reagent), acetic acid (HAc, 99.5%, Macklin), ethanol (C_2H_6O, 99.8%, Sinopharm Chemical Reagent), *N*,*N*-dimethylformamide (DMF, 99.5%, Macklin), anhydrous iron chloride ($FeCl_3$, 99.99% metals basis, Aladdin), hydrofluoric acid (HF, 40.0%, Macklin), commercial Pt/C (20 wt%, Innochem), nafion solution (5 wt%, Sinero). The deionized (DI) water used in experiments is obtain from Milli-Q integral water purification system (Millipore, 18.2 $M\Omega \cdot cm^{-1}$). N_2 (99.99 vol%) was purchased from Changchun Juyang Gases Company.

Synthesis of UiO-66-NH_2 mesoporous nanobowls (UiO-66-NH_2 mesoNBs)

Typically, 100 mg of ODMB, 100 mg of F127, and 60 mg of SDS were dissolved in 12 mL of water under stirring. Subsequently, 270 mg of $ZrOCl_2$ $8H_2O$, 250 mg of NaBr, 3.2 mL HAc, and 100 mg of BDC-NH_2 were added into the above solution. Then, the mixture was stirred at 45 °C and 600 rpm for 24 h. The products were obtained by centrifugation and subsequently washed three times using *N,N*-dimethylformamide and ethanol. To remove the surfactant templates, the as-synthesized samples were soaked in ethanol for 2 days at 50 °C, during which time the ethanol was renewed every day. Finally, the products were dried overnight at 60 °C under vacuum.

Synthesis of UiO-66-NH_2 microporous crystals (UiO-66-NH_2 microCs)

It was synthesized based on the previous report with some modifications.[1] Typically, 102 mg of $ZrCl_4$, 72.5 mg of BDC-NH_2, and 6 mL of acetic acid were dissolved in 50 mL of DMF at room temperature and 600 rpm for 15 min. The mixture was then sealed up and heated in an oven at 120 °C for 24 h. The as-synthesized UiO-66 crystals were washed with DMF and ethanol and then dried in a vacuum oven at 60 °C for 12 h.

Synthesis of iron/nitrogen-doped carbon mesoporous nanobowls (Fe–N–C mesoNBs)

Typically, 60 mg of anhydrous $FeCl_3$ was positioned at the upstream end of a porcelain boat, while 30 mg of UiO-66-NH_2 mesoNBs powder was placed at the downstream side.[2] The boat was then heated to 400 °C under an N_2 atmosphere at a rate of 5 °C min^{-1} and maintained at that temperature for 2 hours. Subsequently, the temperature was raised to 900 °C at the rate of 5 °C min^{-1} and held for another 2 hours for pyrolysis before being cooled to room temperature. After that, the black powder was dispersed in HF (20 wt%) solution for 24 hours standing. The black sample was collected through centrifugation, followed by multiple washes with distilled water and ethanol, and then dried overnight under a vacuum at 60 °C.

Synthesis of iron/nitrogen-doped carbon (Fe–N–C particles)

Fe–N–C particles were prepared by using UiO-66-NH_2 MicroCs as the carbon support. The procedures used to prepare Fe–N–C particles were otherwise identical to that described for Fe–N–C mesoNBs.

Synthesis of nitrogen-doped carbon mesoporous nanobowls (N–C mesoNBs)

The synthesis route of N–C mesoNBs is similar to the Fe–N–C mesoNBs, with the only difference being the absence of the iron precursor.

Characterizations

The powder X-ray diffraction measurements were performed on a Rigaku D-Max 2550 diffractometer by using Cu Kα radiation. The 2θ angle of the diffractometer was stepped from 5° to 50° at a scan rate of 5°/min. Scanning electron microscopy images were measured with Hitachi SU8020 and JEOL JSM-7800F electron microscopes at the energy of of 3 kV, respectively. The transmission electron microscopy images and the elemental mapping were acquired with Talos F200S and Tecnai F20 electron microscopes at an accelerating voltage of 200 kV, respectively. Nitrogen adsorption and desorption measurements were performed using a Micromeritics ASAP 3-flex analyzer at 77 K, following the degassing of the samples at 120 °C for 12 hours under vacuum. The electrospray ionization-mass spectroscopy (ESI-MS) was carried out on Agilent 1290-6545XT mass spectrometer. Small-Angle X-ray Scattering (SAXS) measurements were conducted using a Xeuss 3.0 equipped with a Cu Kα microfocus source. Ultraviolet-visible (UV-Vis) spectra were obtained with a Shimadzu UV-2450 spectrometer. Raman spectra were analyzed using a LabRAM HR Evolution. X-ray

Photoelectron Spectroscopy (XPS) measurements were executed on a Thermo ESCALAB 250, utilizing Al Kα radiation as the X-ray source. For the XPS analyses, the C 1s spectra of externally contaminated carbon was used as the reference peak for calibration. First, we calibrated the characteristic peak of -C-C/C-H at 284.8 eV. The difference between the measured value and the reference value (284.8 eV) was then used as the charge correction value to correct the binding energies of other elements in the XPS spectra. The contact angles (CAs) were analyzed by an optical contact angle meter (DSA100, KRUSS) at ambient conditions (temperature: 23–25 ℃), and each value was obtained by measuring three different positions. Zeta potential was measured at 25 °C on the Malvern ZS-90 Zetasizer instrument.

Electrochemical Measurements

The ink of all catalysts was prepared by dispersing 5 mg of catalyst in 1 mL of mixed solvent containing 50 μL of Nafion solution and ethyl alcohol. The ink was prepared by sonication for at least 30 min. 20 μL of ink was dropped on the rotating disk electrode (RDE) glass carbon electrode with a diameter of 5 mm, and 25 μL of ink was dropped on the rotating ring-disk electrode (RRDE) glass carbon electrode with a diameter of 5.6 mm.

Electrochemical measurements were performed using a traditional three-electrode system on a Chenhua CHI660E electrochemical workstation at room temperature. This includes a glassy carbon RDE or RRDE as a working electrode, a carbon rod as a counter electrode, and a saturated calomel electrode as a reference electrode. The ORR tests were performed in an O_2/N_2 saturated 0.1 M KOH electrolyte. The potentials reported in this work were calibrated to the RHE using the conversion $E_{RHE} = E_{SCE} + 0.0592 \times pH + 0.242$. After that, LSVs were obtained at different rotation rates (400, 625, 900, 1225, 1600, and 2025 rpm) at 10 mV s^{-1} and room temperature. RRDE measurements were carried out at rotating speeds at 1600 rpm and the ring potential was constant at 1.5 V. Finally, stability testing was carried out at $E_{1/2}$ for 30000 s and methanol poisoning testing was measured at 500 s.

The H_2O_2 yield (H_2O_2%) and electron transfer number (n) were calculated by the following equations:

$$n = \frac{4I_D}{I_D + I_R/N}$$

$$H_2O_2\% = \frac{I_R/N}{I_D + I_R/N} \times 200\%$$

Where I_D is the disk current; I_R is the ring current, and N is the collection efficiency of the ring current (0.37 in this work).

The K-L equations can be used to analyze kinetic parameters as following:

$$\frac{1}{J} = \frac{1}{J_K} + \frac{1}{J_L} = \frac{1}{J_K} + \frac{1}{B\omega^{1/2}}$$

$$B = 0.2nFC_0(D_0)^{2/3}\upsilon^{-1/6}$$

Where J represents the measured current density, J_K is the kinetic current density, J_L is the limiting diffusion current density, ω is the electrode rotating rate, F is the Faraday constant (96485 C mol^{-1}), C_0 is the bulk concentration of O_2 0.1 M KOH (1.26×10^{-6} mol cm^{-3}), D_0 is the oxygen diffusion coefficient (1.9×10^{-5} cm^2 s^{-1}) of 0.1 M KOH, and ν is the kinematic viscosity of 0.1 M KOH (0.01 cm^2 s^{-1}).

Finite-Element Simulation Methods

Two-dimensional models were applied to explore the fluid flow behaviors through the different porous structures. The model of Fe–N–C mesoNBs was plotted as a bowl shape (inner radius of 45 nm and thickness of 45 nm) with surface pores of 5 nm. The model of Fe–N–C particles was plotted as a core-shell structure (shell thickness of 6 nm) with surface pores of 1 nm and internal pores of 10 nm. A rectangular area measuring 6000 nm in width and 6010 nm in height was filled with water to establish the computational domain. Given the low Reynolds number regime (Re ≈ 10^{-4}) due to the small size of the Fe–N–C catalysts, the "Laminar Flow" module was employed to simulate the flow field. In the steady-state simulation, the Fe–N–C catalysts were positioned along the upper boundary of the domain to represent their adhesion to an electrode. The left boundary was designated as an inlet with a velocity of 0.235 m s^{-1}, modeling the flow generated by the electrode's rotation. The right boundary was treated as an outlet, while the bottom boundary was set as an open boundary. All remaining boundaries were configured as nonslip boundaries. The flow field was solved by the

Navier−Stokes equations:

$$\nabla \cdot u = 0$$

$$\rho(u \cdot \nabla)u = \nabla \cdot \left[-pI + \mu\left(\nabla u + (\nabla u)^T\right)\right] + F$$

where **u** is the velocity, ρ is the density, **p** is the pressure, and *F* is the volume force vector.

Section 2. Supplementary Figures

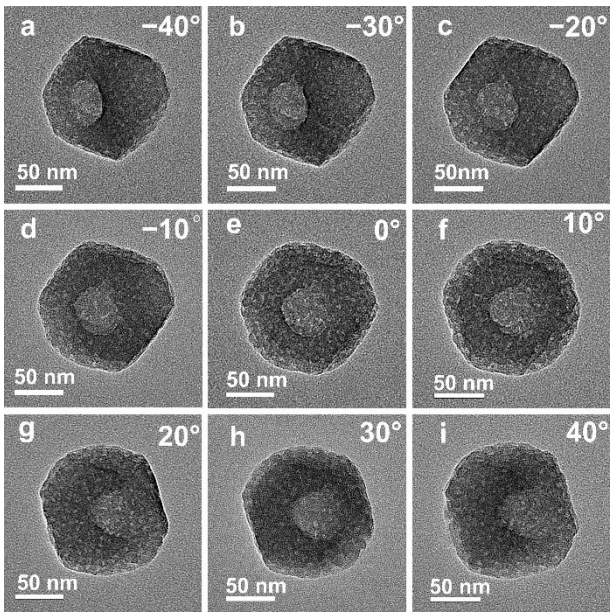

Fig. S1. Tomographic TEM images with different facing directions from (a-i) −40° to 40° of UiO-66-NH_2 mesoNBs.

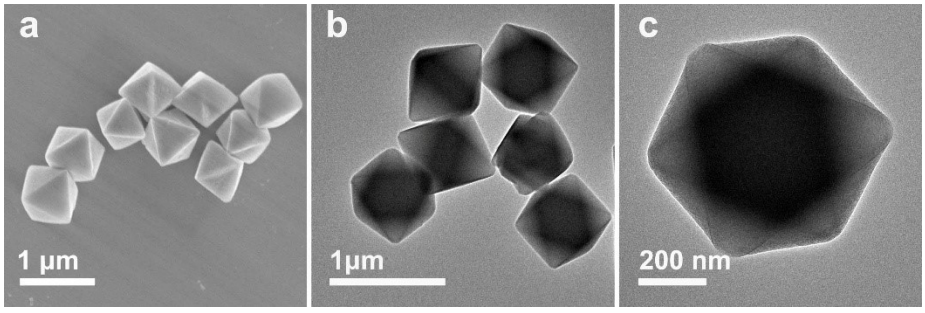

Fig. S2. (a) SEM and (b,c) TEM images of UiO-66-NH_2 microCs.

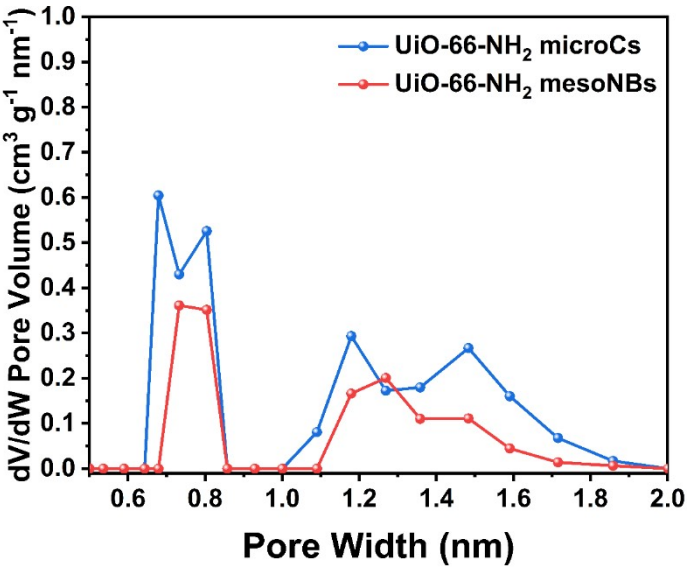

Fig. S3. NLDFT micropore size distributions of UiO-66-NH_2 microCs and UiO-66-NH_2 mesoNBs.

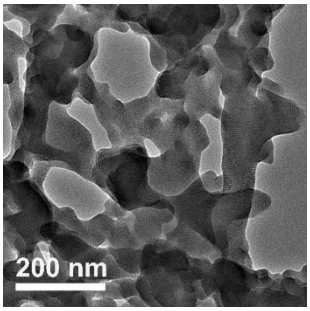

Fig. S4 The TEM image of coralloidal SDS/Zr-oxo clusters complexes.

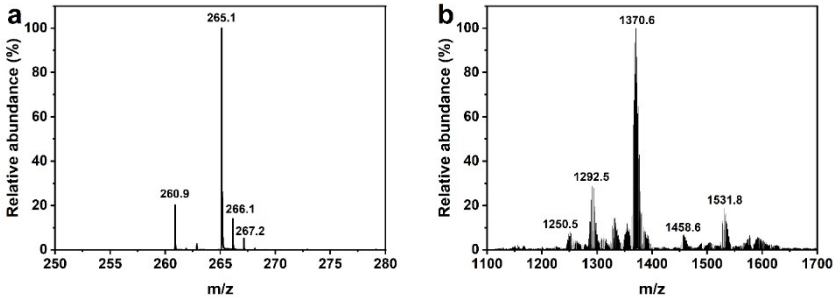

Fig. S5. ESI mass spectra of SDS/Zr-oxo clusters complexes operated in (a) negative-ion mode and (b) positive-ion mode.

Note: The negative ion mass spectra (Fig. S5a) show a single abundant neat SDS anion at m/z 265.1.[3] As shown in Fig. S5b, the positive ion mass spectra observed at m/z 1200-1600 evidenced the presence of Zr_6-oxo clusters.[4]

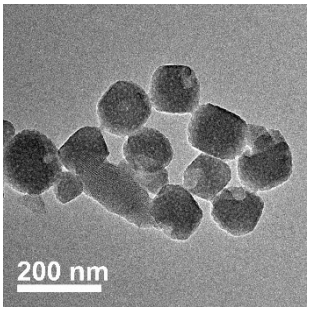

Fig. S6. The TEM image of products obtained after 12 hours during the synthesis of UiO-66-NH_2 mesoNBs.

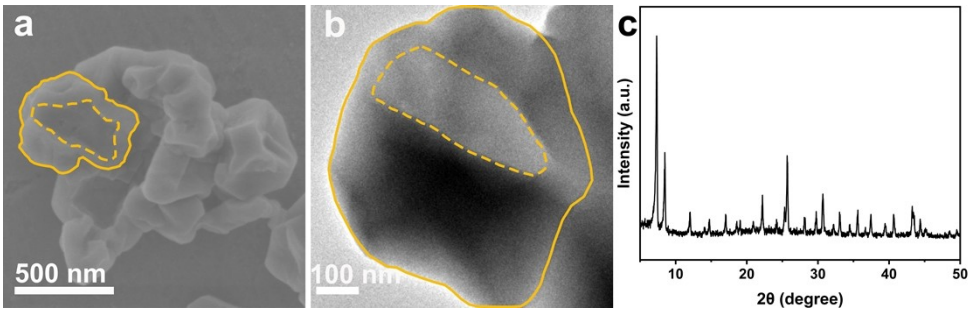

Fig. S7. (a) SEM image, (b) TEM image, and (c) XRD pattern of UiO-66-NH_2 synthesized with SDS templates. The boundaries of the opening and wall in the bowl-shaped nanostructures in panels a and b are profiled by the orange dashed lines and orange solid lines, respectively.

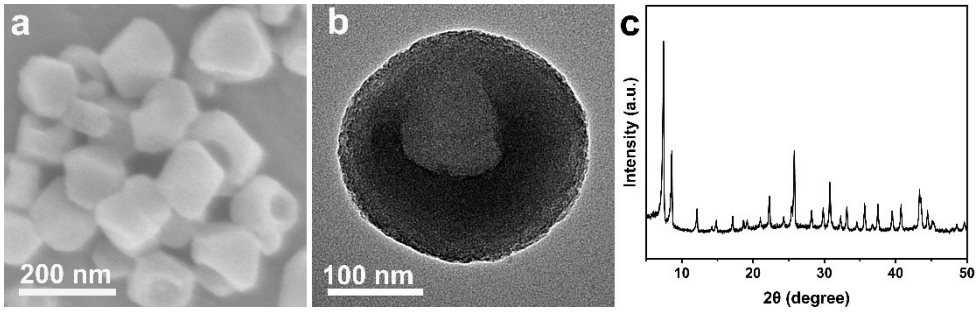

Fig. S8. (a) SEM image, (b) TEM image, and (c) XRD pattern of UiO-66-NH_2 synthesized with F127 and SDS templates.

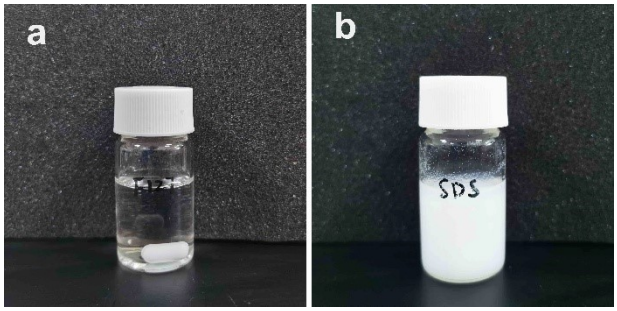

Fig. S9. Digital photos of $ZrOCl_2$ aqueous solution after mixing with different surfactants: (a) F127 and (b) SDS.

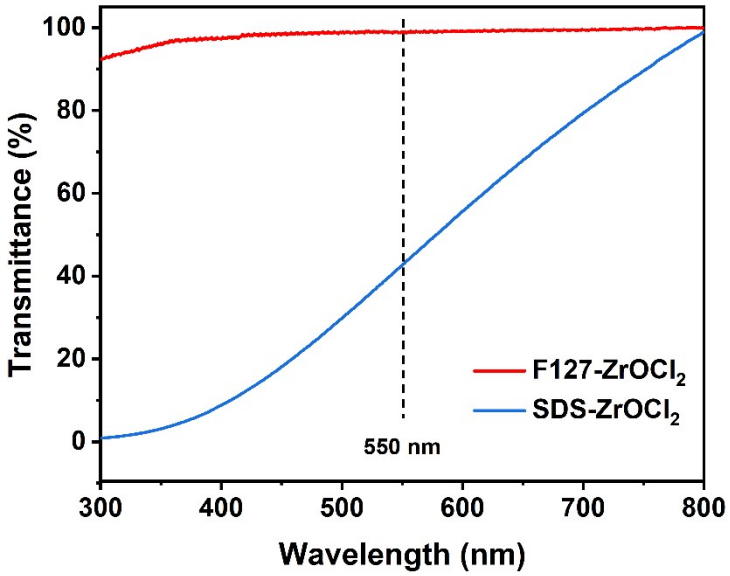

Fig. S10. UV-vis spectra of 1 mM $ZrOCl_2$ aqueous solutions mixed with F127 and SDS, respectively.

Note: We investigated the interaction between two different surfactants and $ZrOCl_2$. The interaction strength was evaluated using turbidity measurements, which detect the formation of aggregates by measuring changes in solution transmittance.[5] Higher turbidity indicates a stronger interaction between the surfactants and the Zr-oxo clusters. The results show that the interaction strength between SDS surfactants and Zr-oxo clusters is greater than that between F127 and Zr-oxo clusters.

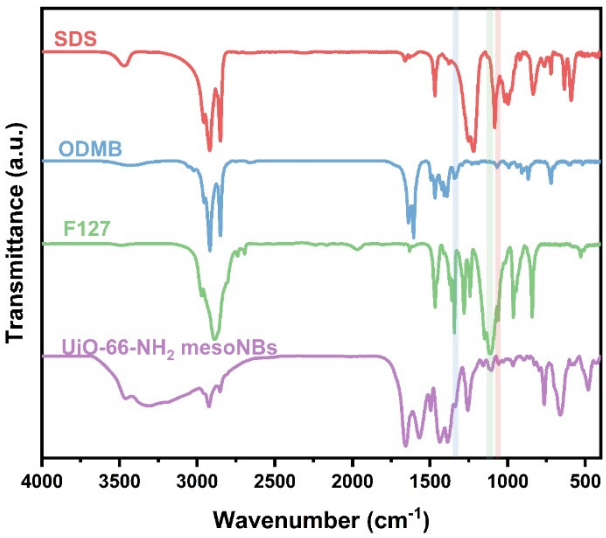

Fig. S11. FTIR spectra of the SDS, ODMB, F127, and UiO-66-NH_2 mesoNBs.

Note: In the FTIR spectrum of UiO-66-NH_2 mesoNBs, the band at 1061 cm^{-1} corresponds to the symmetric (ν_s S–O) stretching of the sulfate group in SDS.[6] Compared to pure SDS, the band of sulfate stretching vibration shifts significantly from 1082 cm^{-1} to 1061 cm^{-1}, which may be attributed to the coordination interaction between SDS and the Zr-oxo clusters. The band centered at 1334 cm^{-1} is assigned to the stretching vibration band of C–N in ODMB.[7] In addition, a peak near 1108 cm^{-1} can be observed in the C−O−C stretching region, which can be attributed to the free ether units of poly(propylene oxide) (PPO) and poly(ethylene oxide) (PEO) groups in the F127 surfactant.[8]

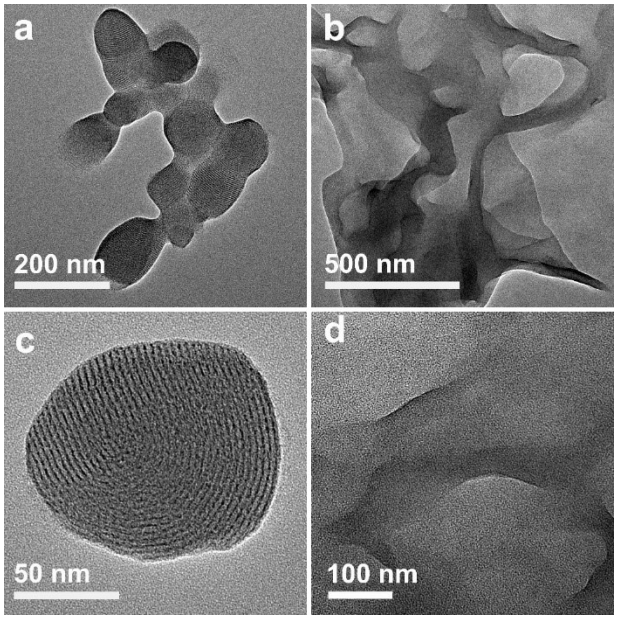

Fig. S12. TEM images of SDS/Zr-oxo clusters complexes obtained at different F127/SDS/ODMB ratios: (a,c) 0.11:0.18:0.71, (b,d) 0.25:0.60:0.15.

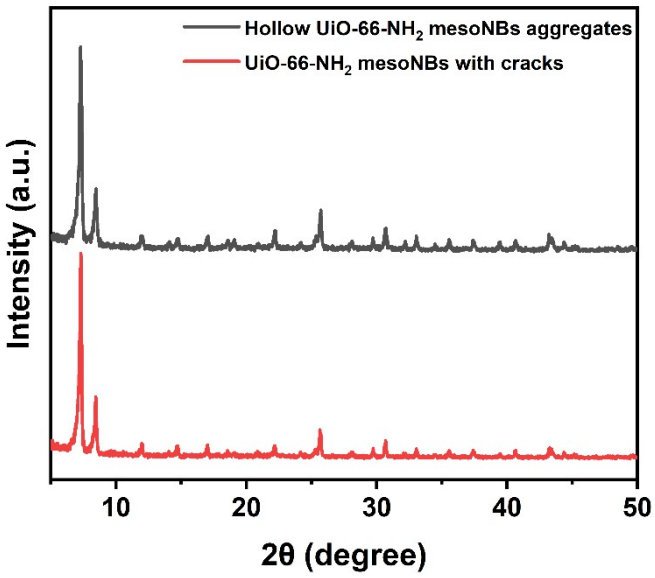

Fig. S13. The XRD patterns of hollow UiO-66-NH_2 mesoNBs aggregates and UiO-66-NH_2 mesoNBs with cracks.

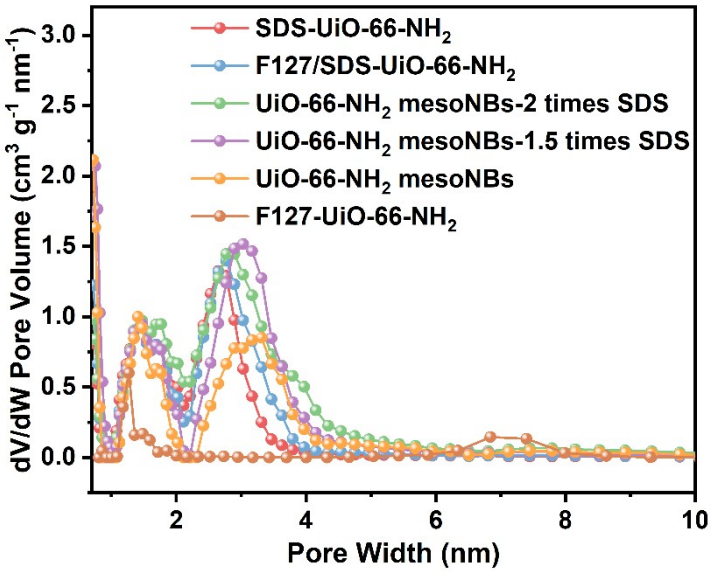

Fig. S14. NLDFT pore size distributions of SDS-UiO-66-NH_2, F127/SDS-UiO-66-NH_2, UiO-66-NH_2 mesoNBs-2 times SDS, UiO-66-NH_2 mesoNBs-1.5 times SDS, UiO-66-NH_2 mesoNBs, and F127-UiO-66-NH_2.

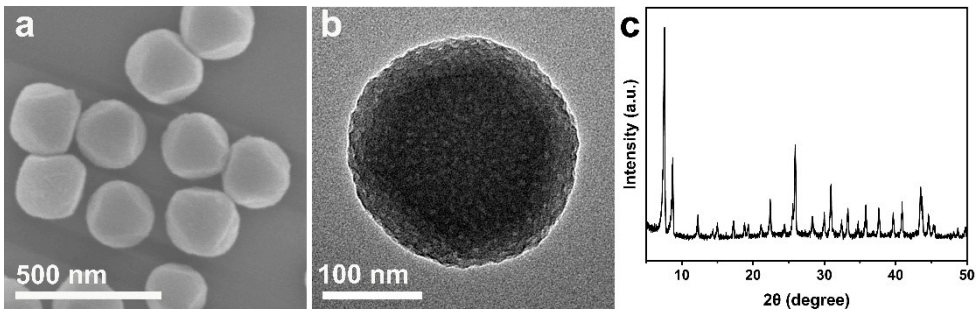

Fig. S15. (a) SEM image, (b) TEM image, and (c) XRD pattern of UiO-66-NH_2 synthesized with F127 templates.

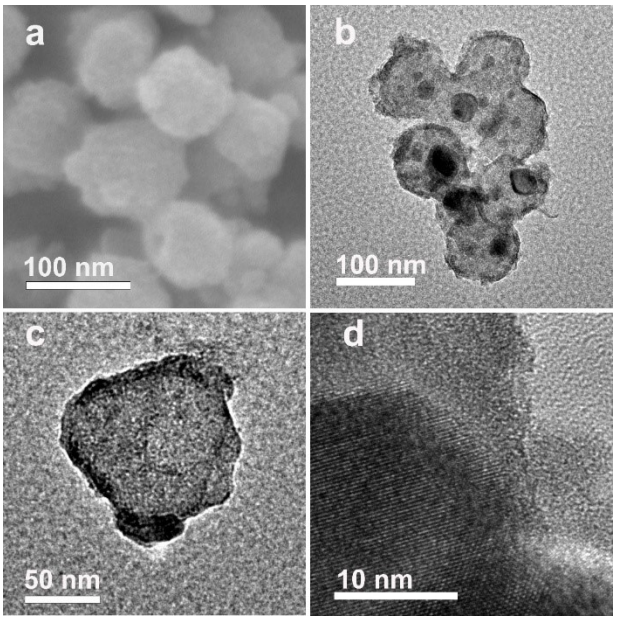

Fig. S16. (a) SEM and (b-d) TEM images of ZrO_2/Fe NPs & Fe–N–C mesoNBs.

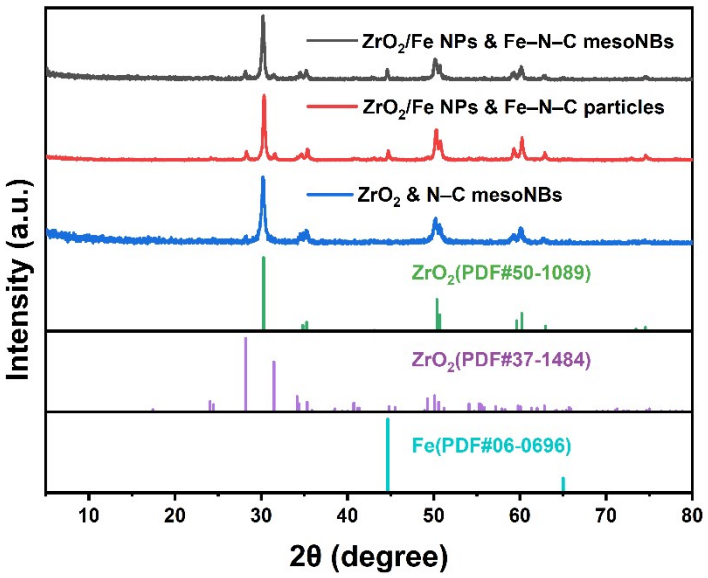

Fig. S17. XRD patterns of ZrO_2/Fe NPs & Fe–N–C mesoNBs, ZrO_2/Fe NPs & Fe–N–C particles, and ZrO_2 & N–C mesoNBs.

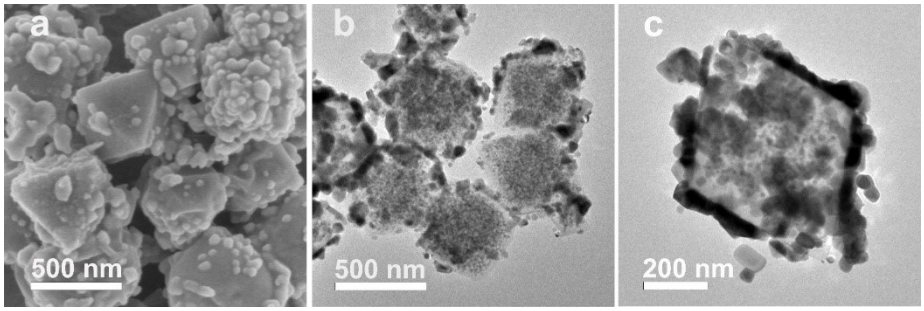

Fig. S18. (a) SEM and (b,c) TEM images of ZrO_2/Fe NPs & Fe–N–C particles.

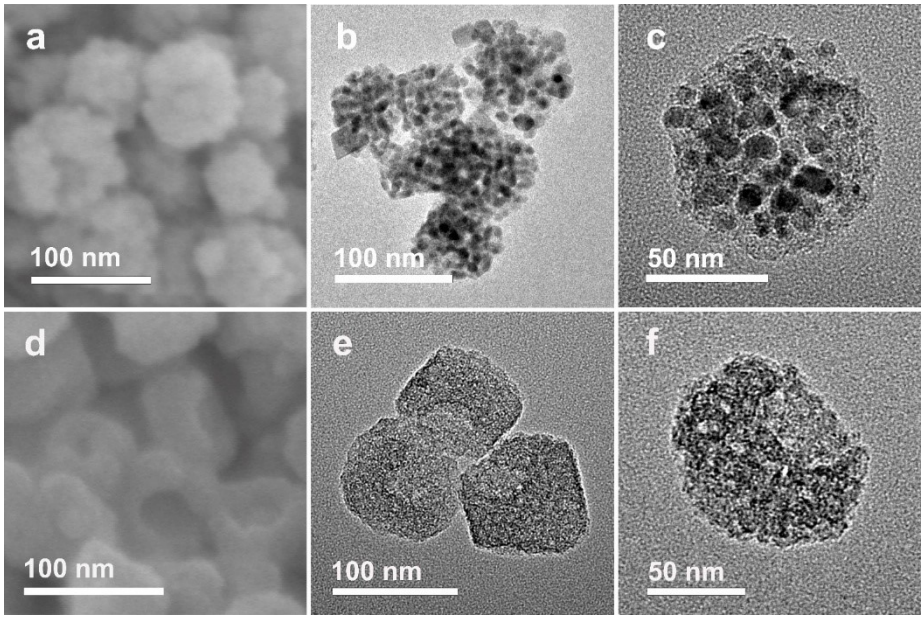

Fig. S19. (a) SEM and (b,c) TEM images of ZrO_2 & N–C mesoNBs. (d) SEM and (e,f) TEM images of N–C mesoNBs.

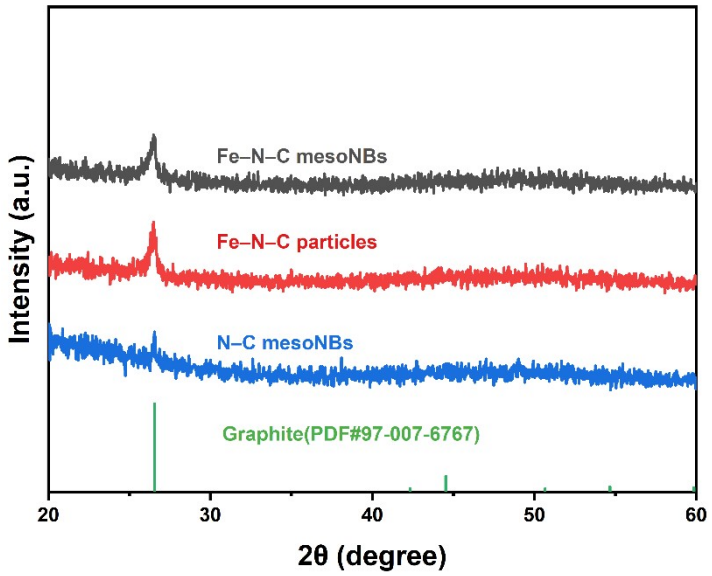

Fig. S20. XRD patterns of Fe–N–C mesoNBs, Fe–N–C particles, and N–C mesoNBs.

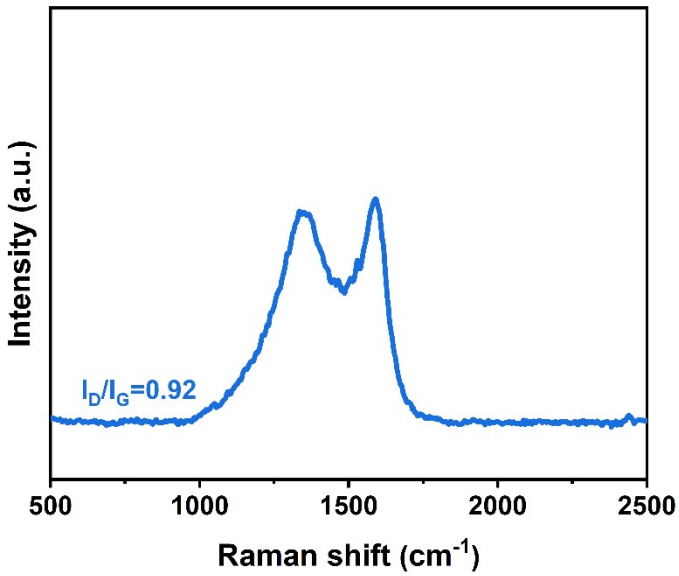

Fig. S21. Raman spectrum of N−C mesoNBs.

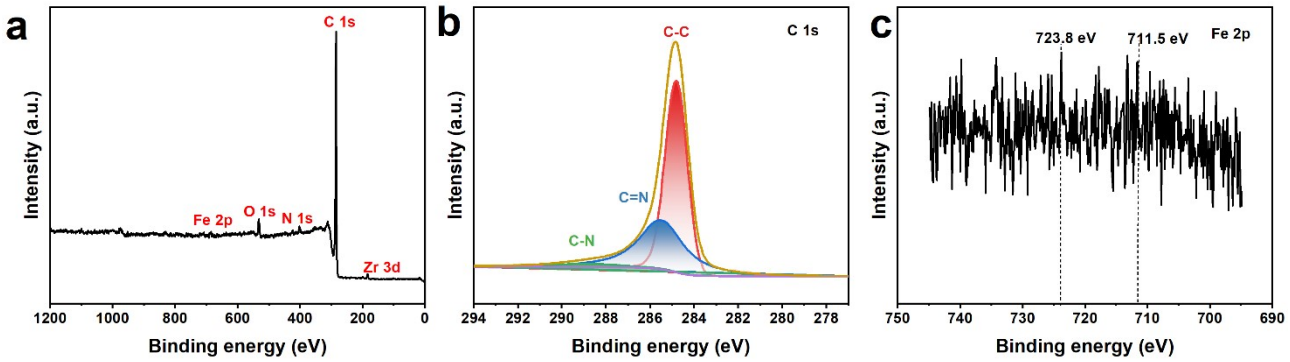

Fig. S22. (a) Survey XPS spectrum, high-resolution (b) C 1s, and (c) Fe 2p spectra of Fe–N–C mesoNBs.

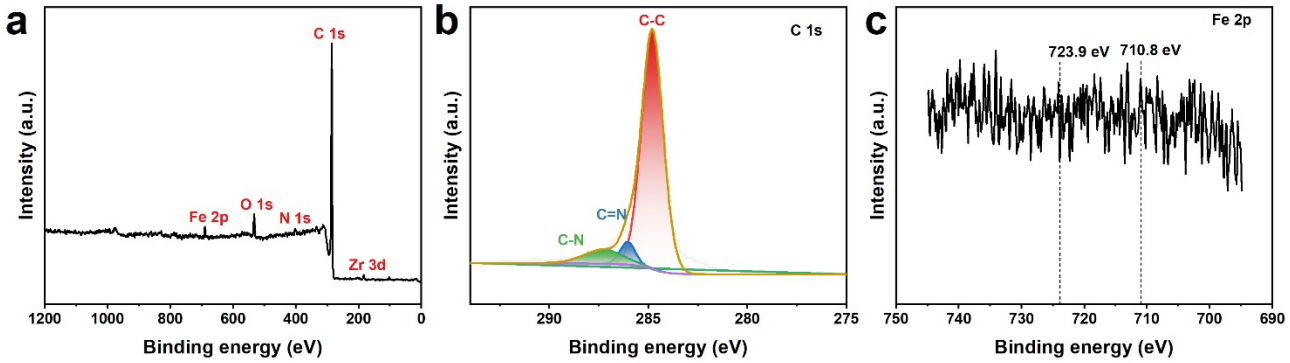

Fig. S23. (a) Survey XPS spectrum, high-resolution (b) C 1s, and (c) Fe 2p spectra of Fe–N–C particles.

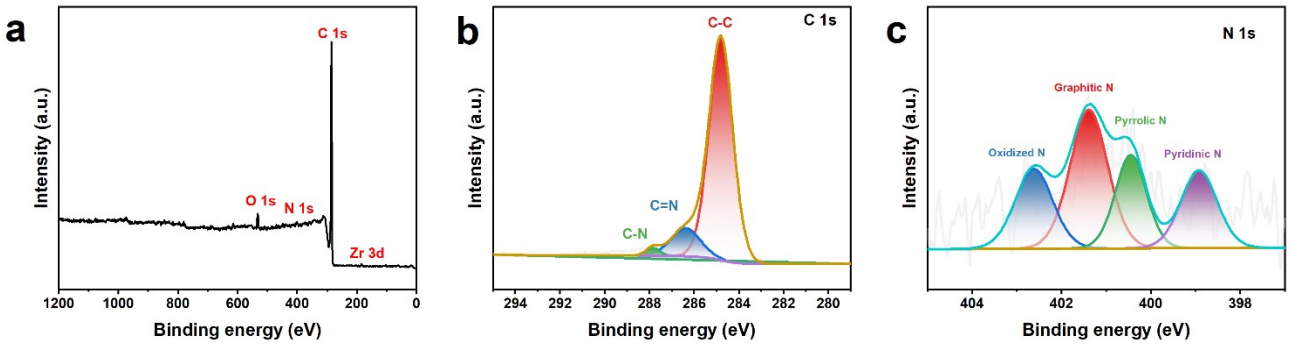

Fig. S24. (a) Survey XPS spectrum, high-resolution (b) C 1s, and (c) N 1s spectra of N–C mesoNBs.

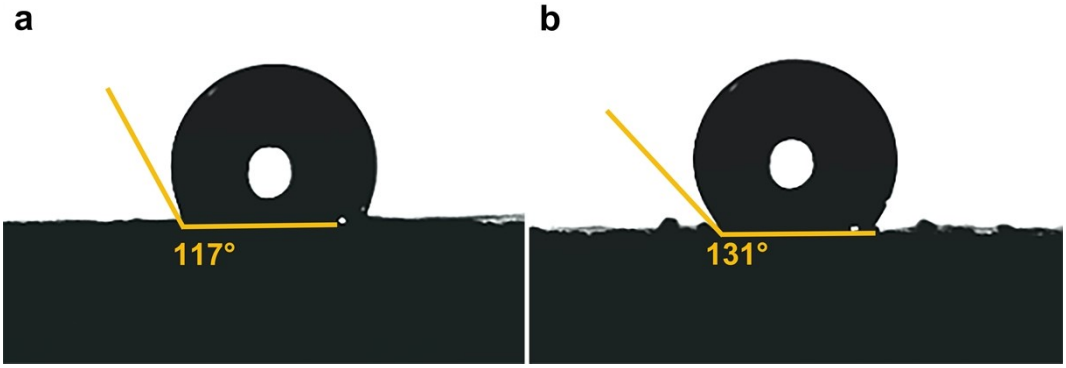

Fig S25. The contact angle tests of (a) Fe−N−C mesoNBs and (b) Fe–N–C particles.

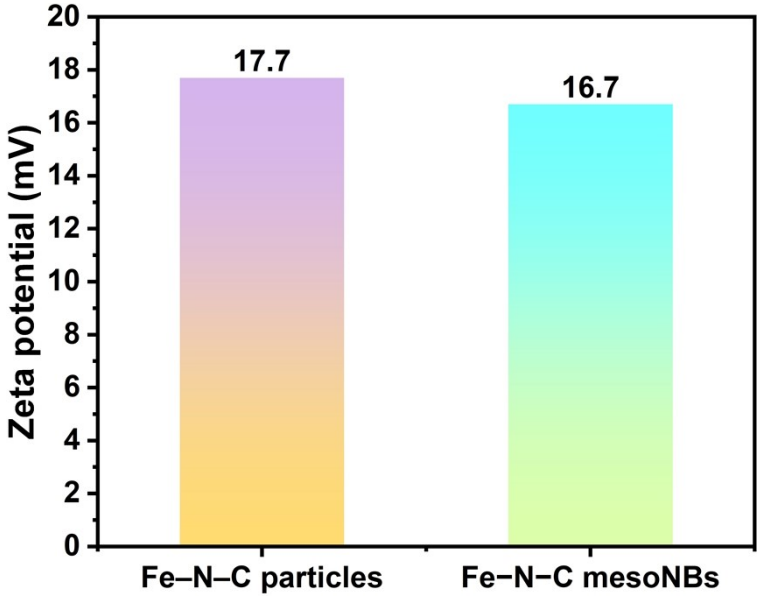

Fig. S26. The surface zeta potential tests of Fe−N−C mesoNBs and Fe–N–C particles.

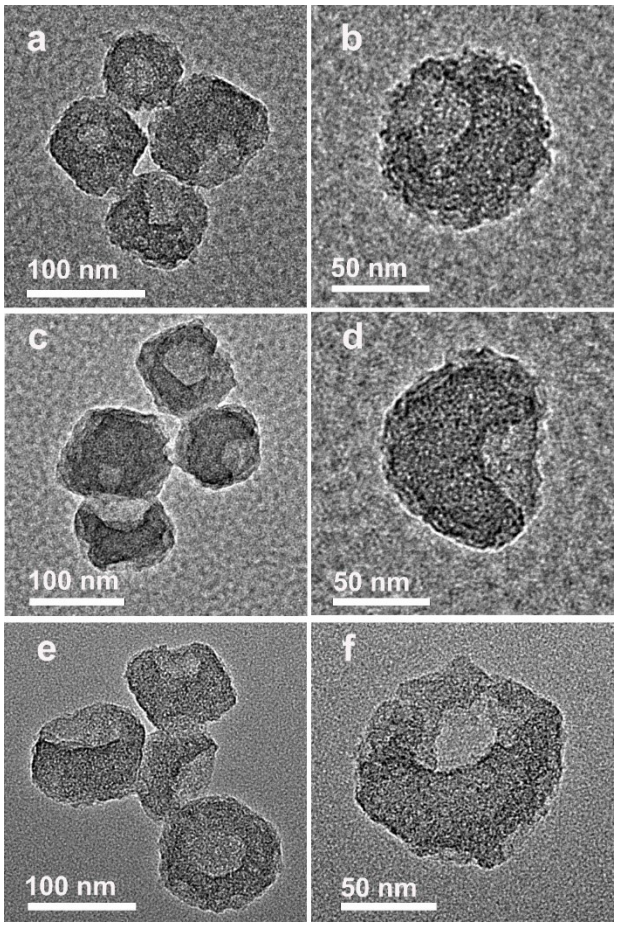

Fig. S27. TEM images for (a, b) Fe–N–C mesoNBs-800, (c, d) Fe–N–C mesoNBs-1000, and (e,f) Fe–N–C mesoNBs-1100.

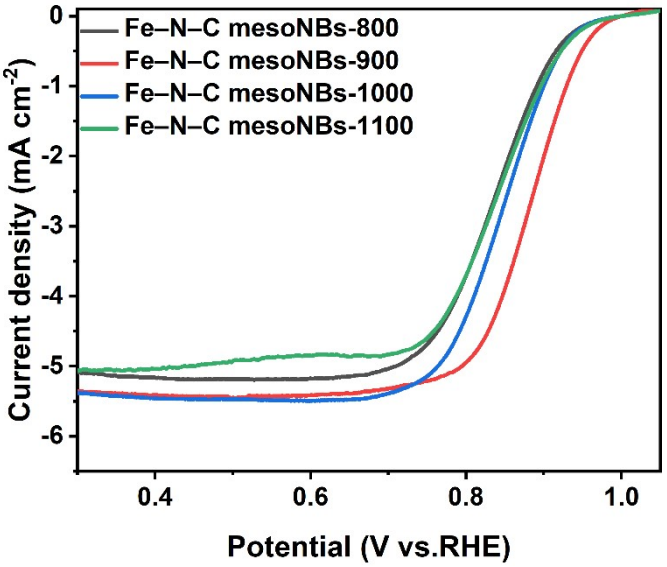

Fig. S28. LSV curves for Fe–N–C mesoNBs-T (T represents the calcination temperature) in O_2-saturated 0.1 M KOH with a rotating rate of 1600 rpm after 95% iR correction.

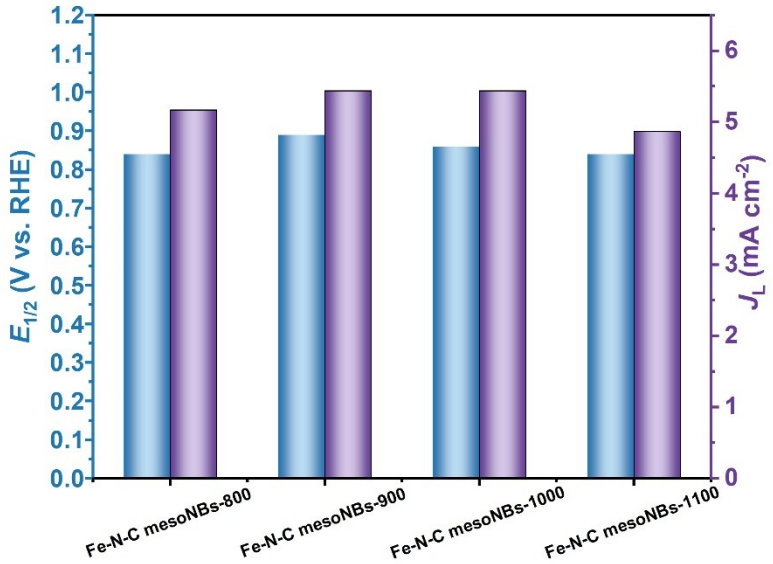

Fig. S29. Comparison of half-wave potential ($E_{1/2}$) and limiting current density (J_L) at 0.90 V for different Fe–N–C mesoNBs-T electrocatalysts in O_2-saturated 0.1 M KOH.

Note: Fe-N-C mesoNBs-T produced at 900 °C exhibited the highest activity with a $E_{1/2}$ of 0.89 V and a J_L of 5.44 mA cm^{-2}.

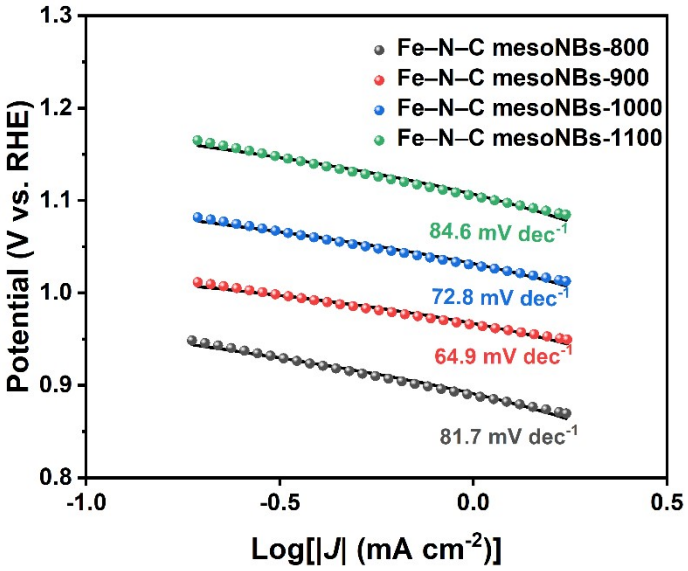

Fig. S30. Tafel plots for Fe–N–C mesoNBs-T electrocatalysts in O_2-saturated 0.1 M KOH.

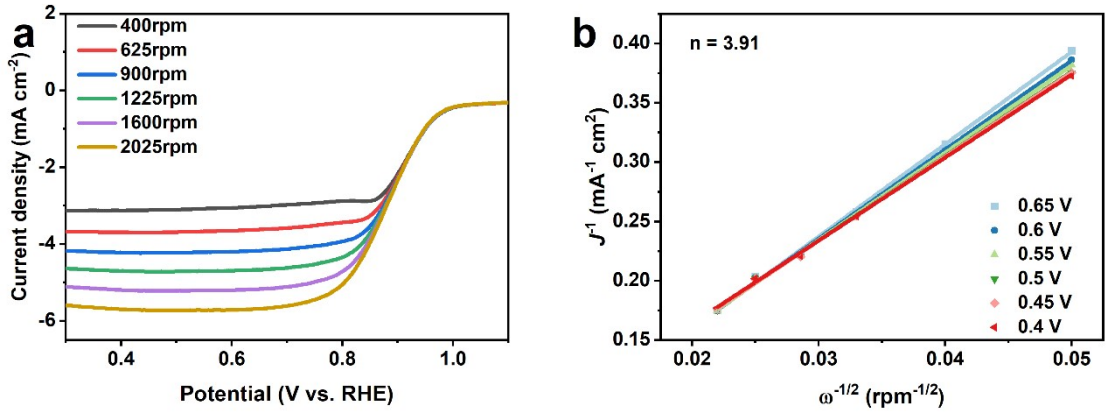

Fig. S31. (a) The polarization curves at different rotating speeds and (b) the corresponding K-L plots of Fe–N–C mesoNBs.

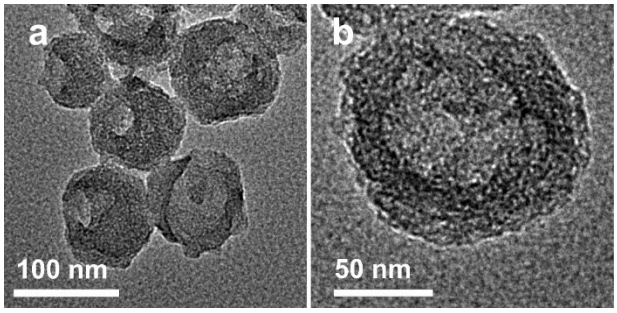

Fig. S32. (a,b) TEM images of Fe–N–C mesoNBs after 5000 cycles.

Section 3. Supplementary Tables

Table S1. Textural properties for UiO-66-NH_2 mesoNBs and UiO-66-NH_2 microCs.

Samples	S_{BET} [a] ($m^2\ g^{-1}$)	V_{meso} [b] ($cm^3\ g^{-1}$)	V_{total} [c] ($cm^3\ g^{-1}$)
UiO-66-NH_2 mesoNBs	667	0.258	0.674
UiO-66-NH_2 microCs	818	-	0.414

[a]S_{BET} (total surface area) calculated by applying the BET equation using the linear part (0.05<P/P0<0.30) of the adsorption isotherm.

[b]V_{meso} (mesopore volume) calculated using BJH method.

[c]V_{total} (total pore volume) calculated by single point adsorption total pore volume of pores at P/P_0=0.99.

Table S2. Fe, N, and C contents in the Fe–N–C mesoNB and Fe–N–C particles.

Samples	Fe [a] (at%)	N [b] (at%)	C [b] (at%)	N/C ratio [b]
UiO-66-NH_2 mesoNBs	0.1	0.57	99.33	0.006
UiO-66-NH_2 microCs	0.1	0.77	99.13	0.008

[a]The corresponding Fe element content was acquired by energy dispersive spectrometer (EDS) analysis.

[b]The contents of N and C together with the N/C ratio acquired and calculated by CHN analysis.

Table S3. Comparison of ORR performance for Fe–N–C-based catalysts in 0.1 M KOH solution.

Samples	Onset potential (V vs. RHE)	Half-wave potential (V vs. RHE)	Tafel slope (mV dec^{-1})	References
Fe(Fc)–N/S–C	0.991	0.872	66.9	9
Fe_1-HNC-500-850	0.93	0.842	40.0	10
Fe-SAs/NSC	1.00	0.87	60	11
Fe/SNCFs-NH_3	1.02	0.89	70.82	12
Pt_1@Fe–N–C	0.93	0.87	42	13
Fe-N/P-C-700	0.941	0.867	-	14
FeP_x/Fe–N–C/NPC	1.01	0.86	60	15
Fe/OES	1	0.85	-	16
Fe-SAs/NSC	1.04	0.84	54	17
Fe-N_4 SAs/NPC	0.972	0.885	91	18
Fe–N–C mesoNBs	**1.03**	**0.89**	**64.6**	**This work**

Supplementary references

1 J. Yang, F. J. Zhang, X. Wang, D. S. He, G. Wu, Q. H. Yang, X. Hong, Y. Wu and Y. D. Li, *Angew. Chem. Int. Ed.*, 2016, **55**, 12854-12858.

2 L. Jiao, J. K. Li, L. L. Richard, Q. Sun, T. Stracensky, E. R. Liu, M. T. Sougrati, Z. P. Zhao, F. Yang, S. C. Zhong, H. Xu, S. Mukerjee, Y. Huang, D. A. Cullen, J. H. Park, M. Ferrandon, D. J. Myers, F. Jaouen and Q. Y. Jia, *Nat. Mater.*, 2021, **20**, 1385-1391.

3 M. V. Kosevich, V. V. Chagovets, V. S. Shelkovsky, O. A. Boryak, V. V. Orlov, A. Gomory and P. Vegh, *Rapid Commun. Mass Spectrom.*, 2007, **21**, 466-478.

4 S. Dai, C. Simms, I. Dovgaliuk, G. Patriarche, A. Tissot, T. N. Parac-Vogt and C. Serre, *Chem. Mater.*, 2021, **33**, 7057-7066.

5 R. F. P. Pereira, A. J. M. Valente and H. D. Burrows, *J. Colloid Interface Sci.*, 2014, **414**, 66-72.

6 K. V. Padalkar, V. G. Gaikar and V. K. Aswal, *J. Mol. Liq.*, 2009, **144**, 40-49.

7 X. Wang, Z. Q. Zhang, Y. F. Cui, W. Li, C. R. Yang, H. Song, W. Q. Qin and F. Jiao, *Int. J. Miner. Metall. Mater.*, 2024, **31**, 71-80.

8 K. X. Wang, L. P. Yang, H. X. Li and F. Zhang, *ACS Appl. Mater. Interfaces*, 2019, **11**, 21815-21821.

9 X. H. Li, X. X. Yang, L. T. Liu, H. Zhao, Y. W. Li, H. Y. Zhu, Y. Z. Chen, S. W. Guo, Y. N. Liu, Q. Tan and G. Wu, *ACS Catal.*, 2021, **11**, 7450-7459.

10 X. Y. Zhang, S. Zhang, Y. Yang, L. G. Wang, Z. J. Mu, H. S. Zhu, X. Q. Zhu, H. H. Xing, H. Y. Xia, B. L. Huang, J. Li, S. J. Guo and E. K. Wang, *Adv. Mater.*, 2020, **32**, 1906905.

11 J. Q. Zhang, Y. F. Zhao, C. Chen, Y. C. Huang, C. L. Dong, C. J. Chen, R. S. Liu, C. Y. Wang, K. Yan, Y. D. Li and G. X. Wang, *J. Am. Chem. Soc.*, 2019, **141**, 20118-20126.

12 L. P. Yang, X. Zhang, L. X. Yu, J. H. Hou, Z. Zhou and R. T. Lv, *Adv. Mater.*, 2022, **34**, 2105410.

13 X. J. Zeng, J. L. Shui, X. F. Liu, Q. T. Liu, Y. C. Li, J. X. Shang, L. R. Zheng and R. H. Yu, *Adv. Energy Mater.*, 2018, **8**, 1701345.

14 K. Yuan, D. Lützenkirchen-Hecht, L. B. Li, L. Shuai, Y. Z. Li, R. Cao, M. Qiu, X. D. Zhuang, M. K. H. Leung, Y. W. Chen and U. Scherf, *J. Am. Chem. Soc.*, 2020, **142**, 2404-2412.

15 Q. Qin, H. Jang, P. Li, B. Yuan, X. Liu and J. Cho, *Adv. Energy Mater.*, 2019, **9**, 1803312.

16 C. C. Hou, L. L. Zou, L. M. Sun, K. X. Zhang, Z. Liu, Y. W. Li, C. X. Li, R. Q. Zou, J. H. Yu and Q. Xu, *Angew. Chem. Int. Ed.*, 2020, **59**, 7384-7389.

17 S. X. Yang, Y. H. Yu, M. L. Dou, Z. P. Zhang, L. M. Dai and F. Wang, *Angew. Chem. Int. Ed.*, 2019, **58**, 14724-

14730.

18 Y. Pan, S. J. Liu, K. A. Sun, X. Chen, B. Wang, K. L. Wu, X. Cao, W. C. Cheong, R. G. Shen, A. J. Han, Z. Chen, L. R. Zheng, J. Luo, Y. Lin, Y. Q. Liu, D. S. Wang, Q. Peng, Q. Zhang, C. Chen and Y. D. Li, *Angew. Chem. Int. Ed.*, 2018, **57**, 8614-8618.